Covalent Organic Frameworks with Carbon-centered Radical Sites for Promoting the 4e⁻ Oxygen Reduction Reaction

Tingting Xu,[2#] Huaqun Zhou,[1#], Xiaofei Zhang,[1*] Tun Seng Herng,[3] Jun Ding,[3] Chi Chunyan,[2*] Jun Zhu[1*]

1. Institute of Materials Research and Engineering (IMRE), Agency for Science, Technology and Research (A*STAR), 2 Fusionopolis Way, Singapore 138634

2. Department of Chemistry, National University of Singapore, 3 Science Drive 3, Singapore 117543

3. Department of Materials Science and Engineering, National University of Singapore, Singapore 119260

# These authors contributed equally to this work.

ABSTRACT: Radical covalent organic frameworks (RCOFs) have demonstrated significant potential in redox catalysis and energy conversion applications. However, the synthesis of stable RCOFs with well-defined neutral carbon radical centers is challenging due to the inherent radical instability, limited synthetic methods and characterization difficulties. Building upon the understanding of stable carbon radicals and structural modulations for preparing crystalline COFs, herein we report the synthesis of a crystalline carbon-centered RCOF through a facile post-oxidation process. Moreover, the RCOF demonstrated outstanding catalytic activity in the 4e⁻ oxygen reduction reaction (ORR) with a half-wave potential of 0.82 V (vs. RHE), among the highest in reported COF-based electrocatalysts. The promoted 4e⁻ and suppressed 2e⁻ ORR pathway (99.5% vs. 0.5%) can be attributed to facilitated reaction initiation and smoother transition steps at the carbon radical sites, which is practically beneficial for minimizing peroxide formation, thus contributing to safer and more sustainable fuel cell and metal-air battery applications. Overall, our study not only provided a facile strategy for preparing stable RCOFs with well-defined neutral carbon radical centers but also demonstrated their capability to fine-tune the redox catalytic activity of COF materials, which could be potentially useful in electrocatalysis and energy conversion applications.

INTRODUCTION

Covalent organic frameworks (COFs) have garnered significant research attention due to their distinctive ordered channel structures, large pore apertures, and exceptional chemical and thermal stability. [1-3] They have demonstrated promising applications in various research fields.[4, 5] While most COFs are closed-shell materials, radical COFs (RCOFs), as an emerging class of materials, are known for their unusual optoelectronic, magnetic, and redox properties owing to the unpaired electrons.[6-8] RCOFs have been identified to show great potential in redox catalysis and energy conversion applications.[9-11]

Oxygen reduction reaction (ORR) is crucial for advancing clean energy technologies, such as fuel cells and metal-air batteries.[12-14] While many COFs have been synthesized using the versatile Schiff base or other nitrogen-containing linkages, they often exhibit a 2e⁻ or mixed ORR pathway that generates peroxides in ORR electrocatalysis (Scheme 1a).[15-19] The 2e⁻ pathway must be suppressed in fuel cell and metal-air battery applications because generation of peroxides can significantly reduce the lifespan and pose safety concerns.[20-22] This issue can be mitigated by adopting redox active COF knots/linkers (Schem 1b, with 5-15% peroxides formation),[23-27] but it faces issues like necessity for more complex and expensive monomers, increased risk of active site poisoning, and limited capability of suppressing peroxide formation.[28-30] Involving neutral carbon radicals in COFs could be a promising alternative strategy.[7] However, the exploration and development have been largely restricted by significant challenges, including inherent instability of carbon radicals, limited synthetic methods and difficulties in characterization.

In principle, RCOFs can be prepared by either direct synthesis or post-synthetic modifications. Direct synthesis involves radical-containing monomers. This method is straightforward but most of potential radical monomers are not stable enough to withstand COF synthetic conditions. More commonly, post-modification method is adopted, where radical species are either grafted onto pre-constructed COFs by chemical modifications or generated *in situ* from pre-constructed COFs by redox reactions. In 2015, Jiang introduced the first radical-containing COF, in which redox active

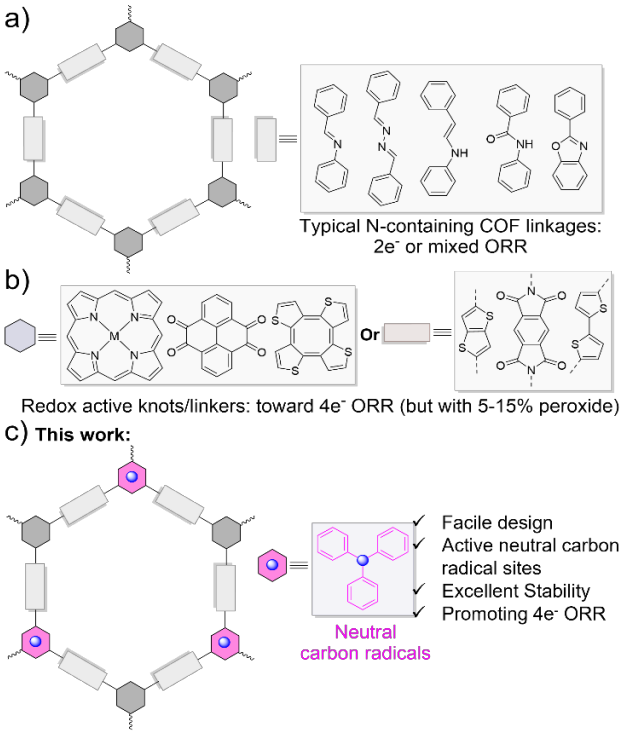

Scheme 1. a) Typical nitrogen-containing COF linkages with 2e⁻ or mixed ORR pathway; b) The reported methods to adopt redox active knots or linkers for encouraging 4e⁻ ORR; c) Our strategy to incorporate carbon radicals for promoting 4e⁻ ORR (efficient 4e⁻ pathway and minimized peroxide production).

TEMPO radicals were immobilized onto the frameworks, resulting in materials with high-performance capacitive energy storage.[9] Meanwhile, monomers were also designed to incorporate TEMPO radicals for the direct synthesis, which exhibited excellent catalytic activity in alcohol oxidation.[11] In contrast to TEMPO-based oxygen-centered RCOFs, carbon-centered RCOFs can be synthesized through chemical redox reactions of pre-constructed COFs containing redox-active moieties, resulting in the formation of carbon radical ions.[6,10,31-33] However, the resulting radical ions are usually sensitive to oxygen and moisture, which restricts their practical applications. Therefore, it is highly desirable to construct RCOFs with stable neutral radical centers.

Triphenylmethyl-based radicals are renowned for their exceptional persistence due to effective spin delocalization and steric protection.[34-36] Their stability and molecular symmetry make them excellent candidates as building monomers for RCOFs. Based on previous studies and ongoing experimental attempts (Figure S1), unsubstituted triphenylmethane has emerged as a more reasonable monomer due to several advantages. The absence of halogen substituents allows for more effective structural packing during COF formation reaction. Besides, triphenylmethyl radicals can be easily generated by organic oxidants without the necessity for strong bases, thereby preserving crystallinity. Although there is some compromise in radical stability, triphenylmethyl radicals are stable enough under many practical conditions.[36-39]

With the above-mentioned considerations in mind, herein we report the facile design and synthesis of a stable crystalline RCOF with neutral carbon radical centers. The structures and properties were thoroughly characterized by various techniques, assisted by *in situ* experiments and theoretical calculations. Moreover, the prepared RCOF demonstrated outstanding catalytic activity in 4e⁻ ORR with a half-wave potential of 0.82 V (vs. RHE), among the highest in reported COF-based electrocatalysts. The promoted 4e⁻ and suppressed 2e⁻ ORR pathway (99.5% vs. 0.5%) can be attributed to facilitated reaction initiation and smoother reaction transitions at the carbon radical sites as compared to closed-shell COFs, which is practically beneficial for minimizing peroxide formation, thus contributing to safer and more sustainable fuel cell and metal-air battery applications. Overall, our study not only provided a facile strategy for preparing stable RCOFs with well-defined carbon radical centers but also demonstrated their capability to fine-tune the redox catalytic activity of COF materials, which could be potentially useful in electrocatalysis and energy conversion applications.

RESULTS AND DISCUSSION

The synthesis started with solvothermal condensation of two carefully selected monomers, namely tris(4-aminophenyl)methane (TAPM) and 1,3,5-tris(4-formylphenyl)benzene (TFPB) (prepared according to reported literatures[40,41]), in a mixture of mesitylene, dioxane and acetic acid at 100 °C for 5 days to afford the precursor **COF-H** (yield: 89%, Figure 1a). Since 2,3-dichloro-5,6-dicyano-1,4-benzoquinone (DDQ) oxidation reaction can occur rapidly (within several minutes) for triphenylmethane-type precursors and prolonged post-treatment can cause not only radical quenching but also deterioration in COF crystallinity, the subsequent oxidation reaction was carefully monitored by (electron spin resonance) ESR technique. For the pristine **COF-H** sample, no observable ESR signal was observed (Figure S2, at 0 min).

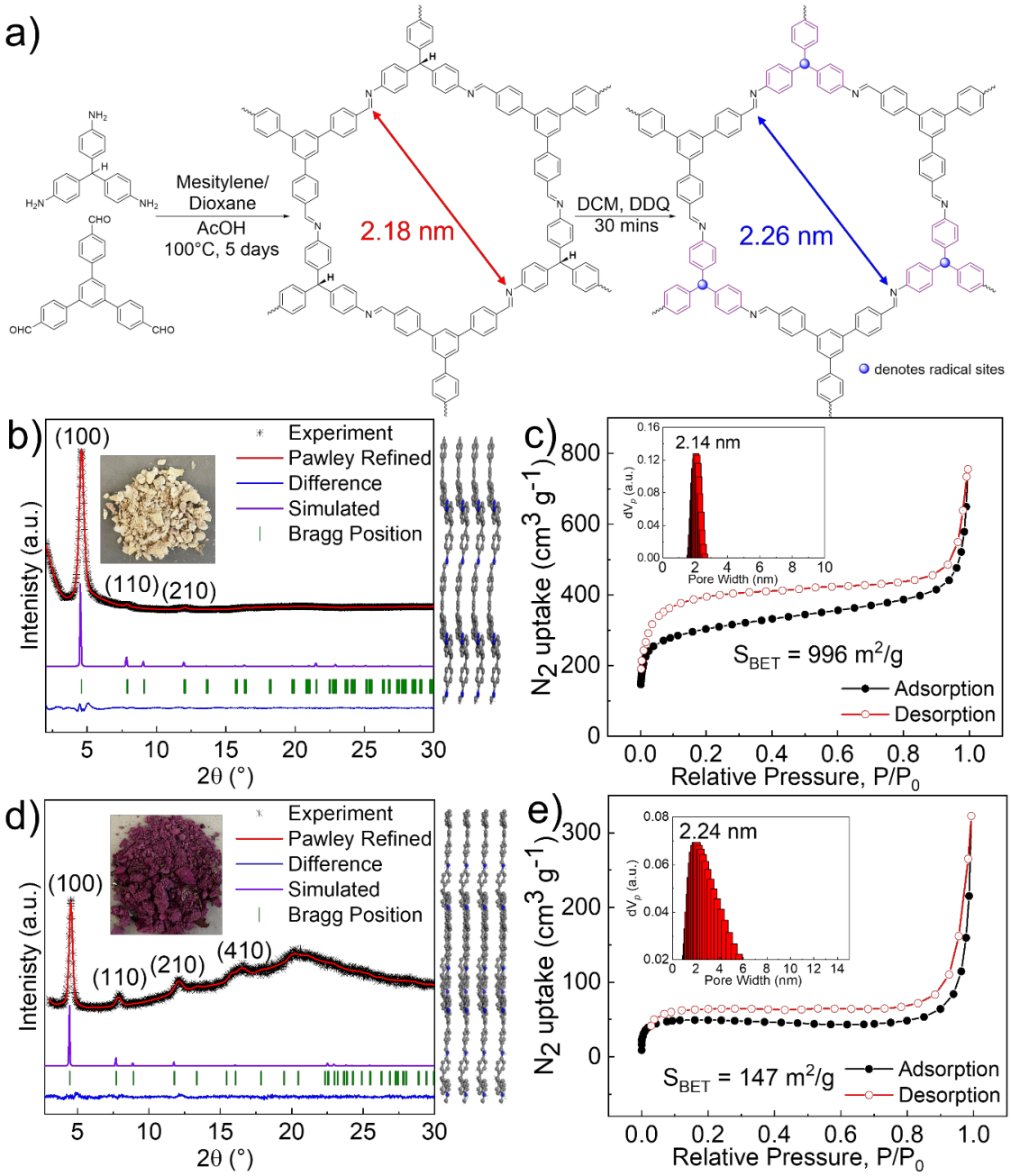

Figure 1. a) Synthetic route of **COF-H** and **COF-R**; b) d) PXRD data of **COF-H** and **COF-R**: experimental (black), Pawley-refined (red), simulated (purple), difference (blue), Bragg position (green); inset is an image of the materials; adjacent illustrates the simulated interlayer packing structure. b) d) BET N_2 sorption isotherm curves of **COF-H** and **COF-R** measured at 77 K: inset is the corresponding pore-size distribution profile.

In contrast, a sharp ESR signal emerged after **COF-H** was treated with DDQ for 5 mins. The ESR signal became more pronounced at 10 mins and was gradually steady after 20-30 mins. No significant signal increase was observed with further increased reaction time. The results suggested that 30-minute treatment of DDQ was sufficient for oxidation to afford **COF-R** (yield: 98 %).

The optical image of **COF-H** shows a pale yellow solid while it is purple for **COF-R** (the insets in Figure 1b and 1d), indicating successful radical generation. The chemical identities of **COF-H** and **COF-R** were analyzed by Fourier transform infrared spectroscopy (FTIR) and ^{13}C cross-polarization magic angle spinning (CP-MAS) NMR spectroscopy. In the solid-state ^{13}C NMR spectrum (Figure S3), the characteristic peak at 157.7 ppm in the low-field region indicated the formation of C=N bonds in **COF-H** and the peak in the high-field region at 54.5 ppm corresponded to the sp^3-hybridized carbons that were ready for radical generation. The ^{13}C

NMR spectrum of **COF-R** was not obtained due to the paramagnetic character of monoradicals.[42,43] Comparing the FTIR spectra (Figure S4) of monomers, **COF-H** and **COF-R**, it was observed that the characteristic sp^3 C-H stretch (2983 cm^{-1} in TAPM and 2988 cm^{-1} in **COF-H**) was significantly weakened in **COF-R**, implying effective oxidation reaction for radical generation.

Comparison of powder X-ray diffraction (PXRD) patterns between the pristine **COF-H** and **COF-R** illustrated that the crystallinity was largely preserved after DDQ oxidation (Figure S5), though a noticeable bump appeared in the region of high reflection angles, which implies the structural packing (mostly π-stacking) could be disrupted by the oxidation process. The first reflection peak of **COF-R** appeared at a slightly lower reflection angle as compared with that of **COF-H** (4.50° vs 4.56°). As the sp^3-hybridized C-H was converted to sp^2-hybridized carbon radical, the triphenylmethyl radical moieties needed to adapt to a more planar conformation, inevitably inducing a small expansion to the original crystal cell and resulting in a slight PXRD peak shift to lower reflection angles. A more detailed crystallographic analysis was performed by comparing the experimental and simulated PXRD patterns (Figure 1b and 1d). The reflection at 4.56°, 7.86°, and 12.08° for **COF-H** can be attributed to (100), (110) and (210) plane, respectively. Good agreement was found between the simulated PXRD pattern and experimentally measured pattern. Pawley refinement was performed, resulting in the unit cell parameters of a = 22.52 Å, b = 22.65 Å, c = 4.23 Å, α = 90°, β =90°, γ =120°, with agreement factors of R_{wp} = 3.12%, R_p = 2.27%. The reflection at 4.50°, 7.81°, 12.04° and 16.42° for **COF-R** can be attributed to (100), (110), (210) and (410) plane, respectively. Good agreement was observed between the simulated PXRD pattern and experimentally measured pattern. Pawley refinement resulted unit cell parameters of a = 23.01 Å, b = 23.01 Å, c = 3.95 Å, α = 90°, β =90°, γ =120°, with agreement factors of R_{wp} = 3.85%, R_p = 2.63%. The interlayer packing structure of **COF-H** appeared slightly wavy due to the presence of sp^3-hybridized carbons while it became more planar for **COF-R** because of the conversion of sp^3-hybridized C-H to sp^2-hybridized carbon radical (Figure 1b and 1d: the insets at right).

The permanent porosity and pore size distribution of **COF-H** and **COF-R** were investigated by nitrogen physisorption analysis at 77 K. The Brunauer-Emmett-Teller (BET) surface areas were determined to be 996 m^2/g and 147 m^2/g, respectively for **COF-H** and **COF-R** (Figure 1c, 1e, and S6). Both isotherms displayed a rise in the low-pressure range, generating a typical type-I nitrogen-sorption isotherm. The pore size distribution determined by non-local density function theory showed a size distribution profile centered at 2.14 nm and 2.24 nm, respectively for **COF-H** and **COF-R**, which agreed well with the pore sizes calculated from optimized geometries (Figure 1a, 2.18 nm and 2.26 nm, respectively for **COF-H** and **COF-R**). Comparing these results, **COF-R** displayed a significant decrease in BET surface area and its pore size distribution also appeared wider than that of the **COF-H**, which could be due to the disrupted structural packing during radical generation.

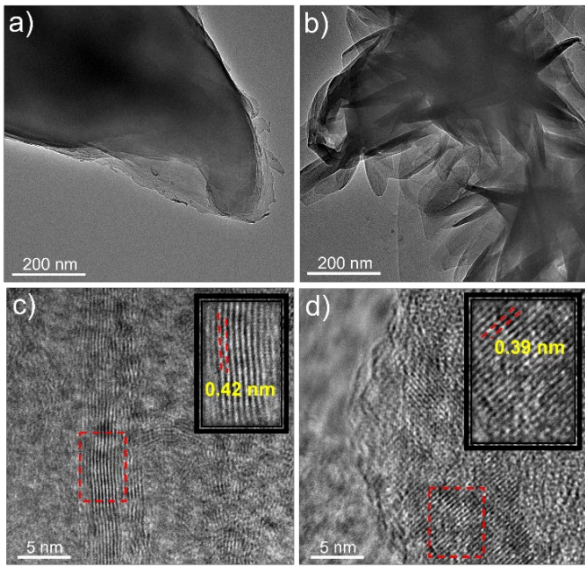

Figure 2. a) c) TEM and HR-TEM images of **COF-H**; b) d) TEM and HR-TEM images of **COF-R**; Insets in HR-TEM images show the enlarged images of the red-marked area with lattice fringes corresponding to the interlayer distances.

The scanning electron microscopy (SEM) images (Figure S7) revealed a plate-like morphology for **COF-H** while **COF-R** looked fluffier (or more swollen). Similar morphologies were also observed in their transmission electron microscopy (TEM) images (Figure 2a and 2b) in which **COF-H** displayed a densely packed layered structure while **COF-R** appeared more loosely packed (or

more exfoliated), which could explain the bump in its PXRD pattern and decreased BET surface area. High resolution TEM (HR-TEM) images (Figure 2c and 2d) confirmed the good crystallinity of **COF-H** and **COF-R** as indicated by the clear lattice fringes which correspond to the interlayer distances (0.42 nm for **COF-H** and 0.39 nm for **COF-R**).

The electron spin resonance (ESR) spectra of **COF-R** showed an intense resonance signal with a *g* value of 2.0027 (Figure 3a), indicating the presence of carbon radicals. The spin density distribution of carbon radicals in **COF-R** (Figure S8) showed the unpaired electrons mainly reside on the tertiary carbon and are partially delocalized into the nearby phenyl rings. To further confirm and quantify the generated carbon radicals, a superconducting quantum interference device (SQUID) technique was employed. The field-dependent magnetization (M vs. applied field B) curves of **COF-H** and **COF-R** were measured at 2 K (Figure S9). As the magnitude of applied field (B) was increasing, **COF-R** demonstrated substantial increase of the magnetization as compared to that of **COF-H**, indicating presence of stable spins in **COF-R** due to the unpaired electrons. The temperature-dependent magnetization of **COF-R** was measured to further investigate its magnetic behavior. As temperature was decreasing, the magnetization steeply increased, indicating a typical behavior of paramagnetic materials (Figure S10). As the saturation behavior can be observed at high magnetic field at 2 K for paramagnetic **COF-R** (Figure S9), it is feasible to quantify the spin concentration by field-dependent magnetization curves at different temperatures from 300 K to 2 K (Figure S11). The obtained Brillouin function fit using scaling parameter of $\mu_B B/k_b T$ (Equation S1) indicated a magnetization saturation of 5.85 emu/g (Figure S12). Therefore, the molar magnetization was calculated to be 3686 emu/mol based on the unit cell of **COF-R** ($C_{46}H_{35}N_3$, molecular weight of 630g/mol). In principle, the magnetization of $S = \frac{1}{2}$ spin is 5586 emu/mol,[8] thus it can be estimated that at least 66% of **COF-H** was successfully converted to **COF-R** with a spin concentration of 3.97×10^{23} spins/mol, which is a high radical content.

The solid-state diffuse reflectance UV-vis spectra of **COF-H** displayed a single absorption peak at 390 nm while **COF-R** showed a new broad absorption band peaked at 563 nm and a long tail extending beyond 800 nm (Figure 3b), which can be attributed to the SOMO-to-LUMO transitions of radical species (SOMO: singly occupied molecular orbital; LUMO: lowest unoccupied molecular orbital). The cyclic voltammogram of **COF-R** in the solid state showed an irreversible reduction wave with onset at -0.75 V and a quasi-reversible oxidation wave with onset at 0.19 V, with respect to Fc/Fc^+ (Figure S13b; Fc: ferrocene). Therefore, the LUMO and HOMO (highest occupied molecular orbital) of **COF-R** was determined to be -4.05 eV and -4.99 eV, respectively, with a small energy gap of 0.94 eV. Similarly, the LUMO and HOMO of **COF-H** was determined to be -2.24 eV and -5.06 eV, respectively, with a large energy gap of 2.82 eV (Figure S13a).

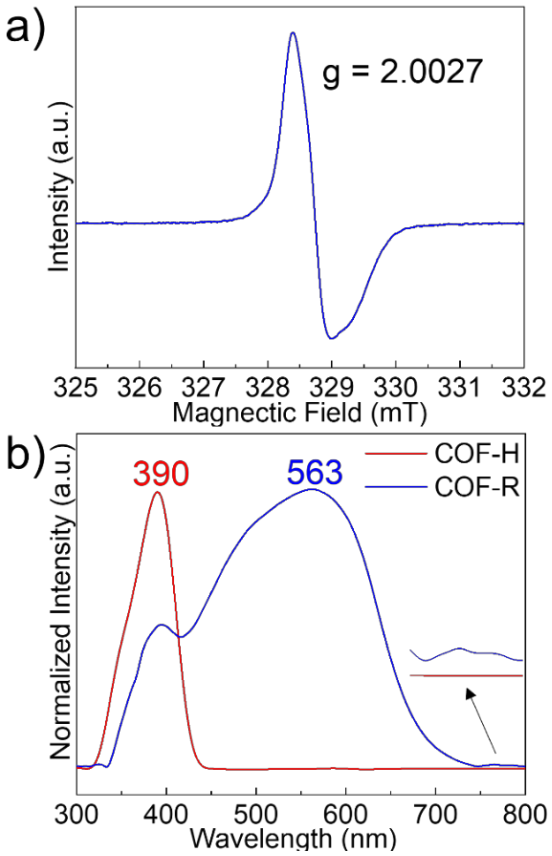

Figure 3. a) ESR spectrum of the solid sample of **COF-R**; b) Solid-state diffuse reflectance UV-vis spectra of **COF-H** and **COF-R**.

Carbon radical species have been discovered to spontaneously reduce O_2.[44] The low-lying LUMO energy level of **COF-R** can be energetically favorable in accepting and transferring electrons in electrocatalysis. Moreover, the small energy gap could facilitate kinetic stability and electrochemical reactivity.[45] Therefore, **COF-R** could be a promising ORR electrocatalyst. The stability of **COF-R**

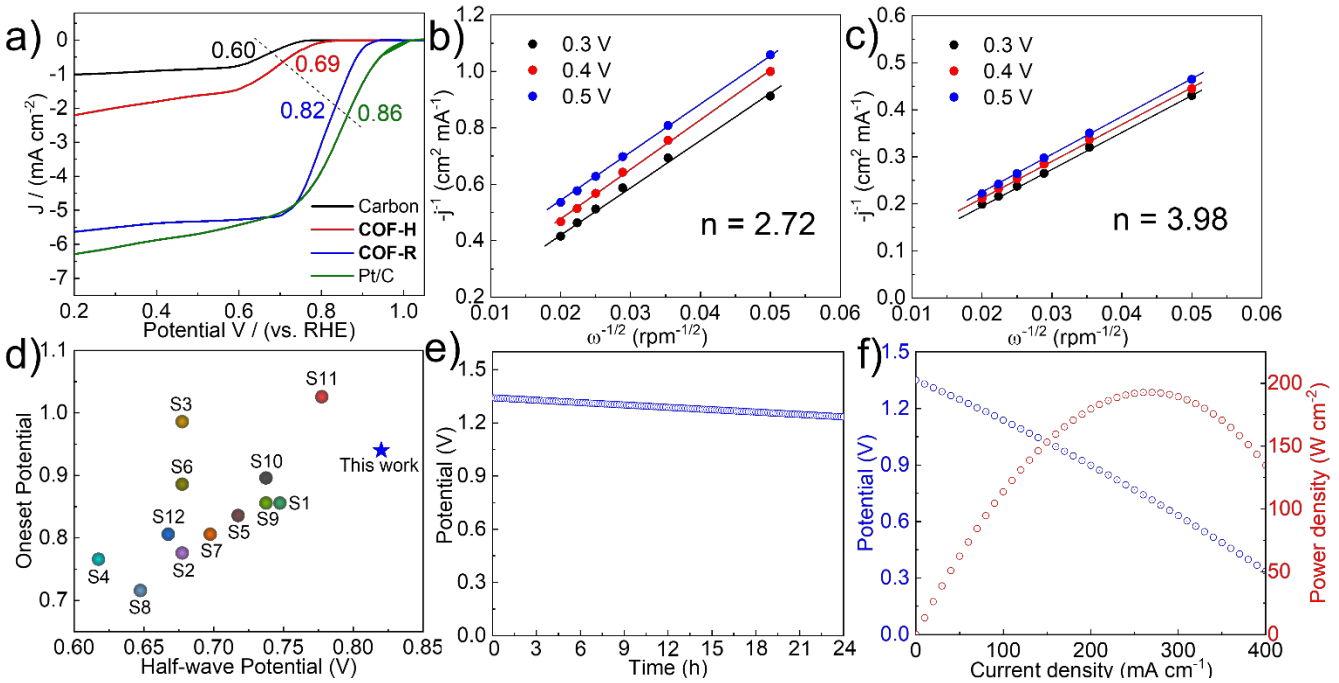

Figure 4. a) The LSV curves (at 1600 rpm) of carbon black, **COF-H**, **COF-R** and Pt/C in O_2-saturated 0.1 M KOH electrolyte; b) c) The Koutecky–Levich (K–L) plots of **COF-H** and **COF-R** at 0.3, 0.4 and 0.5 V; d) The comparison of half-wave and onset potentials between **COF-R** and reported COFs as metal-free ORR electrocatalysts; e) The discharge curve (at a current density of 10 mA cm^{-2}) of a Zn-air battery using **COF-R** as the cathode electrocatalyst; f) The charge polarization and power density curves of the Zn-air battery using **COF-R** as the electrocatalyst layer.

was evaluated in 0.1 M KOH aqueous solution. After 3 days, it can be observed that both the crystallinity and radical concentration of **COF-R** largely remained (Figure S14 and S15), indicating its excellent stability in practical alkaline condition. The good stability of **COF-R** in alkaline condition can be attributed to both the inherent stability of triphenylmethyl radicals and the hydrophobic framework backbones. Besides, thermogravimetric analysis (TGA) demonstrated good thermal stability of **COF-R** with 5% weight loss at 285 °C (Figure S16).

20 wt% of carbon black was added to **COF-H** and **COF-R** to improve both their conductivity and compatibility with aqueous electrolyte during the investigation of their ORR activities. Subsequently, their linear sweep voltammetry (LSV) curves were obtained at different rotation rates (400 to 2500 rpm) in oxygen-saturated 0.1 M KOH aqueous electrolyte (Figure S17 and S18). Besides, LSV of carbon black and commercial 20 wt% Pt/C catalysts were also measured for comparison. The half-wave potentials of carbon black, **COF-H**, **COF-R** and Pt/C were determined to be 0.60, 0.69, 0.82 and 0.85 V (vs. RHE), respectively, from their LSV curves measured at 1600 rpm (Figure 4a). In general, both **COF-H** and **COF-R** displayed more positive halfwave potentials (0.69 and 0.82 V) than that of carbon black (0.60 V). More importantly, both the halfwave potential and limiting current density of **COF-R** (0.82 V and 5.63 mA/cm^2) is very close to that of commercial Pt/C (0.85 V and 6.19 mA/cm^2), illustrating its excellent ORR activity as a metal free electrocatalyst. Comparing to various reported COFs for ORR electrocatalysis, **COF-R** dementated enhanced ORR activity with respect to both half-wave and onset potentials (Figure 4d and Table S2), suggesting that the presence of radical species can largely fine-tune catalytic activity of COF materials. Furthermore, the smaller Tafel slope of **COF-R** (65.6 mV/dec) compared to that of **COF-H** (79.5 mV/dec) indicated the faster reaction kinetics of **COF-R** in catalyzing ORR (Figure S19). The electrochemical impedance measurements revealed that **COF-R** exhibited smaller charge-transporting resistance (Figure S20), which is beneficial for the ORR process. The lower impedance of **COF-R** could be attributed to the stacking of neutral carbon radicals. The corresponding electron transfer numbers (n) of **COF-H** and **COF-R** extracted from Koutecky-Levich (K-L) plots (at 0.3, 0.4 and 0.5 V) were 2.72 and 3.98 (Figure 4b and 4c), respectively, indicating the promoted

4e$^-$ ORR pathway for **COF-R**. The electron transfer number and ORR selectivity were further investigated by RRDE LSV curves (Figure S21 and S22). The results confirmed the electron transfer number for **COF-R** was nearly 4 while it was about 3 for **COF-H**. Besides, the peroxide selectivity for **COF-R** was only 0.5 % while it was rather high for **COF-H** (about 65 %). These results, again, evidenced the presence of carbon radical species in COFs can largely promote 4e$^-$ ORR and suppress peroxide generation.

The durability of **COF-R** was evaluated at 0.7 V vs. RHE for 50000 s (Figure S23). The current density was steady and retained upon addition of methanol into the electrolyte solution at 20000 s, indicating the excellent stability and tolerance towards small organic molecules. Considering the excellent catalytic performance and stability of **COF-R** in ORR process, its application potential was further investigated in an aqueous zinc-air battery (Figure S24). It can be observed that approximately 98% of the initial voltage was maintained after being discharged for 24 h (Figure 4e). The battery demonstrated an open circuit voltage of 1.34 V and a peak power density of 194 mW cm^{-2} (Figure 4f), indicating its excellent performance as a cathode electrocatalytic material and great potential in energy conversion applications.

The active sites in typical Schiff base COFs (mostly identified to be the carbon atoms in C=N bonds) typically adapt to a 2e$^-$ or mixed ORR pathway.[46] However, **COF-R** demonstrated high electrocatalytic activity in promoting the 4e$^-$ ORR pathway, which can be attributed to the presence of carbon radicals. Comprehensive *in situ* experiments and DFT calculations were performed for a thorough investigation to understand the promoted 4e$^-$ ORR catalytic activity and selectivity for **COF-R**. The *in situ* attenuated total reflectance Fourier transform infrared spectroscopy (ATR-FTIR) was employed to elucidate the reaction pathway. Analysis of the spectrum evolution for **COF-H** under open circuit potential (OCP) and a range of applied potentials (1.0 to 0.2 V vs. RHE) revealed prominent peaks at 1025 and 1213 cm^{-1} (Figure 5a), which can be attributed to the *OO$^-$ anion and *HOO intermediates, respectively.[47] In contrast, several key ORR intermediates were observed in the case of **COF-R** (Figure 5b). A small peak at 1045 cm^{-1} corresponding to *OO$^\bullet$ radical intermediate,[48] was located, suggesting the C$^\bullet$ radical sites readily reduced O_2 to form *OO$^\bullet$ intermediate. The peak at 1209 cm^{-1} corresponding to *HOO intermediate suggested the reduction and protonation of *OO$^\bullet$ radical intermediate to form *HOO. The peak at 1354 cm^{-1} could be attributed to the *O$^\bullet$ radical intermediate (C-O$^\bullet$ radical stretch),[49] implying the *HOO intermediate underwent a reductive O-O bond cleavage. The peak at 1165 cm^{-1} indicated the presence of *HO intermediate, which could be resulted from the reduction and protonation of *O$^\bullet$ radical. These results clearly illustrated the more pronounced 4e$^-$ ORR pathway for **COF-R**. Therefore, a plausible 4e$^-$ pathway catalytic cycle was proposed based on the *in situ* experimental results and the typical ORR steps in alkaline electrolyte where H_2O acts as the proton donor (Figure 5c, Table S1).[50] Firstly, O_2 interacts with the active carbon radical site and gets adsorbed, forming the*OO$^\bullet$ radical intermediate. Subsequently, the first electron transfer occurs, accompanied by protonation to form the *OOH intermediate. The reductive O-O bond cleavage by the second electron transfer produces *O$^\bullet$ radical, which then undergoes the third electron transfer and protonation to form the *OH intermediate. During the fourth electron transfer, dissociative reduction occurs, regenerating the active carbon radical site and allowing the initiation of the next catalytic cycle.

Since both the radical carbons and carbons in C=N bonds can serve as the potential active catalytic sites for ORR, their energy diagrams were constructed based on these two different active sites (Figure 5d). At the equilibrium potential (U = 1.23 V), it can be observed at the C=N carbon site that the O_2 → HOO* and HOO* → O* steps are endothermic while O* → HO* and HO* → OH$^-$ steps are exothermic, with O_2 → HOO* being the rate-determining step composing an energy barrier of 1.29 eV. For the radical carbon site, HOO* → O* and OH* → OH$^-$ steps are endothermic while O_2 → HOO* and O* → HO* steps are exothermic, with HOO* → O* being the rate-determining step composing an energy barrier of 1.20 eV. Comparing the energy diagrams at two sites, the O_2 → HOO* step showed significant difference. O_2 → HOO* at the C=N carbon site requires an activation energy to proceed, while it is essentially spontaneous at the carbon radical site because the carbon radical centers more readily interact with O_2 due to the low-lying LUMOs that are mainly distributed around the radical carbon sites (Figure S25). This major difference reveals, on one side, that

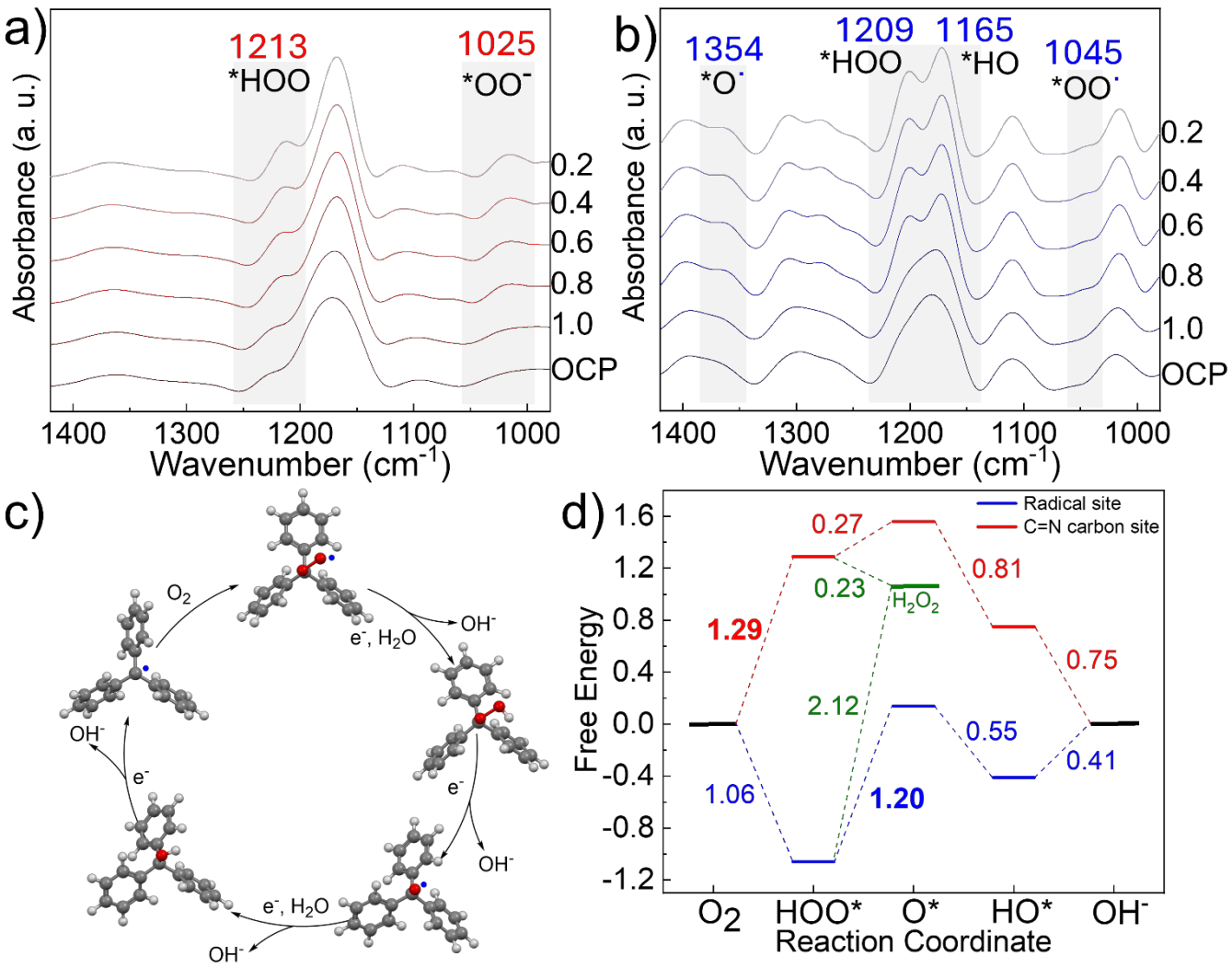

Figure 5. a) b) The in situ ATR-FTIR spectra of COF-H and COF-R measured in 0.1 M KOH electrolyte from 1.0 to 0.2 V (vs RHE); c) Free energy diagram constructed based on different active sites: Radical carbon sites (blue) and C=N carbon site (red) at U = 1.23 V; d) Proposed ORR mechanism and catalytic cycle; * denotes the active site of catalyst;

the radical carbon sites can largely facilitate the ORR initiation step. One the other side, it has subsequently caused the following HOO* reduction step to adapt to distinct reaction pathways. At the C=N carbon site, an energy barrier (0.27 eV) needs to be overcome for HOO* → O* step while it is more spontaneous to yield H_2O_2, thereby it favors a $2e^-$ transfer pathway. In contrast, there is a rather significant energy barrier (2.12 eV) for HOO* → H_2O_2 step at the radical carbon site, thus it goes through a smoother HOO* → O* step in a $4e^-$ transfer pathway.

CONCLUSION

In summary, we have demonstrated the facile design and synthesis of a highly crystalline RCOF with stable neutral carbon radical centers through post-oxidation of a pre-constructed closed-shell precursor COF. **COF-R** has been thoroughly characterized by various techniques, including UV-vis, PXRD, ESR, and SQUID, assisted by *in situ* experiments and theoretical calculations, confirming the presence of stable neutral carbon radicals with a spin concentration of 3.97×10^{23} spins/mol. Besides, **COF-R** demonstrated outstanding catalytic activity in $4e^-$ ORR with a half-wave potential of 0.82 V (vs. RHE), among the highest in reported COF-based electrocatalysts. The promoted 4e- and suppressed 2e- ORR pathway (99.5% vs 0.5%) can be attributed to facilitated reaction initiation and smoother reaction transitions at carbon radical sites as compared to closed-shell COFs. Further investigation of **COF-R** as cathode catalyst layer in an aqueous zinc-air battery showed an

open circuit voltage of 1.34 V and a peak power density of 194 mW cm^{-2}. Overall, our study not only provided a facile strategy to prepare stable RCOFs with well-defined neutral carbon radical centers but also demonstrated their great potential for electrocatalysis and energy conversion applications.

ASSOCIATED CONTENT

Supporting Information. The Supporting information is available free of charge at.

AUTHOR INFORMATION

Corresponding Author

Jun Zhu - Institute of Materials Research and Engineering (IMRE), Agency for Science, Technology and Research (A*STAR), 2 Fusionopolis Way, Singapore 138634; Orcid.org/0009-0009-9735-9151.
Email: zhuj@imre.a-star.edu.sg

Chunyan Chi - Department of Chemistry, National University of Singapore, 3 Science Drive 3, Singapore 117543; Email: chmcc@nus.edu.sg

Xiaofei Zhang - Institute of Materials Research and Engineering (IMRE), Agency for Science, Technology and Research (A*STAR), 2 Fusionopolis Way, Singapore 138634.
Email: Xiaofei@imre.a-star.edu.sg

Author Contributions

T. X and H. Z contributed equally to this work.

ACKNOWLEDGMENT

This work was financially supported by Singapore MOE Tier 1 grant (A-8000992-00-00), MOE Tier 2 grant (MOET2EP10222-0008), A*STAR Career Development Fund (C233312013) and A*STAR Young Individual Research Grant (M23M7c0117, M23M7c0118). We acknowledge Dr. Xudong Hou and Dr. Shaofei Wu for their assistance on SQUID measurements and analysis.

REFERENCES

(1) Huang, N.; Wang, P.; Jiang, D. Covalent Organic Frameworks: A Materials Platform for Structural and Functional Designs. *Nat. Rev. Mater.* **2016**, *1*, 16068.

(2 Chen, X.; Geng, K.; Liu, R.; Tan, K. T.; Gong, Y.; Li, Z.; Tao, S.; Jiang, Q.; Jiang, D. Covalent Organic Frameworks: Chemical Approaches to Designer Structures and Built-In Functions. *Angew. Chem. Int. Ed.* **2020**, *59*, 5050-5091.

(3 Tan, K. T.; Ghosh, S.; Wang, Z.; Wen, F.; Rodríguez-San-Miguel, D.; Feng, J.; Huang, N.; Wang, W.; Zamora, F.; Feng, X.; Thomas, A.; Jiang, D. Covalent Organic Frameworks. *Nat. Rev. Methods Primers* **2023**, *3*, 1.

(4) Keller, N.; Bein, T. Optoelectronic Processes in Covalent Organic Frameworks. *Chem. Soc. Rev.* **2021**, *50*, 1813-1845.

(5) Zhao, X.; Pachfule, P.; Thomas, A. Covalent Organic Frameworks (COFs) for Electrochemical Applications. *Chem. Soc. Rev.* **2021**, *50*, 6871-6913.

(6) Jin, E.; Asada, M.; Xu, Q.; Dalapati, S.; Addicoat, M. A.; Brady, M. A.; Xu, H.; Nakamura, T.; Heine, T.; Chen, Q.; Jinag, D. Two-Dimensional sp^2 Carbon–Conjugated Covalent Organic Frameworks. *Science* **2017**, *357*, 673-676.

(7) Wu, S.; Li, M.; Phan, H.; Wang, D.; Herng, T. S.; Ding, J.; Lu, Z.; Wu, J. Toward Two-Dimensional *pi*-Conjugated Covalent Organic Radical Frameworks. *Angew. Chem. Int. Ed.* **2018**, *57*, 8007-8011.

(8) Jiang, Y.; Oh, I.; Joo, S. H.; Buyukcakir, O.; Chen, X.; Lee, S. H.; Huang, M.; Seong, W. K.; Kim, J. H.; Rohde, J. U.; Kwak, S. K.; Yoo, J. W.; Ruoff, R. S. Organic Radical-Linked Covalent Triazine Framework with Paramagnetic Behavior. *ACS Nano* **2019**, *13*, 5251-5258.

(9) Xu, F.; Xu, H.; Chen, X.; Wu, D.; Wu, Y.; Liu, H.; Gu, C.; Fu, R.; Jiang, D., Radical Covalent Organic Frameworks: A General Strategy to Immobilize Open-Accessible Polyradicals for High-Performance Capacitive Energy Storage. *Angew. Chem. Int. Ed.* **2015**, *54*, 6814-8.

(10) Mi, Z.; Yang, P.; Wang, R.; Unruangsri, J.; Yang, W.; Wang, C.; Guo, J. Stable Radical Cation-Containing Covalent Organic Frameworks Exhibiting Remarkable Structure-Enhanced Photothermal Conversion. *J. Am. Chem. Soc.* **2019**, *141*, 14433-14442.

(11) Chen, F.; Guan, X.; Li, H.; Ding, J.; Zhu, L.; Tang, B.; Valtchev, V.; Yan, Y.; Qiu, S.; Fang, Q. Three-Dimensional Radical Covalent Organic Frameworks as Highly Efficient and Stable Catalysts for Selective Oxidation of Alcohols. *Angew. Chem. Int. Ed.* **2021**, *60*, 22230-22235.

(12) Cao, R.; Lee, J. S.; Liu, M.; Cho, J. Recent Progress in Non-Precious Catalysts for Metal-Air Batteries. *Adv. Energy Mater.* **2012**, *2*, 816-829.

(13) Cheng, F.; Chen, J. Metal-Air Batteries: From Oxygen Reduction Electrochemistry to Cathode Catalysts. *Chem. Soc. Rev.* **2012**, *41*, 2172-2192.

(14) Zhang, Q.; Guan, J. Applications of Atomically Dispersed Oxygen Reduction Catalysts in Fuel Cells and Zinc–Air Batteries. *Energy & Environmental Materials* **2020**, *4*, 307-335.

(15) Wu, H.; Li, L.; Chen, H.; Xing, Y.; Wang, Z.; Zhang, C.; Long, X. Topology Control of Covalent Organic Frameworks with Interlaced Unsaturated 2D and Saturated 3D Units for Boosting Electrocatalytic Hydrogen Peroxide Production. *Angew. Chem. Int. Ed.* **2024**, e202410719.

(16) An, S.; Li, X.; Shang, S.; Xu, T.; Yang, S.; Cui, C. X.; Peng, C.; Liu, H.; Xu, Q.; Jiang, Z.; Hu, J. One-Dimensional Covalent Organic Frameworks for the 2e(-) Oxygen Reduction Reaction. *Angew. Chem. Int. Ed.* **2023**, *62*, e202218742.

(17) Yan, X.; Wang, B.; Ren, J.; Long, X.; Yang, D. An Unsaturated Bond Strategy to Regulate Active Centers of Metal-Free Covalent Organic Frameworks for Efficient Oxygen Reduction. *Angew. Chem. Int. Ed.* **2022**, *61*, e202209583.

(18) Guo, Y.; Xu, Q.; Yang, S.; Jiang, Z.; Yu, C.; Zeng, G. Precise Design of Covalent Organic Frameworks for Electrocatalytic Hydrogen Peroxide Production. *Chem. Asian. J.* **2021**, *16*, 498-502.

(19) Deng, M.; Sun, J.; Laemont, A.; Liu, C.; Wang, L.; Bourda, L.; Chakraborty, J.; Van Hecke, K.; Morent, R.; De Geyter, N.; Leus, K.; Chen, H.; Van Der Voort, P. Extending the π-Conjugation System of Covalent Organic Frameworks for More Efficient Photocatalytic H_2O_2 Production. *Green Chemistry* **2023**, *25*, 3069-3076.

(20) Suntivich, J.; Gasteiger, H. A.; Yabuuchi, N.; Nakanishi, H.; Goodenough, J. B.; Shao-Horn, Y. Design Principles for Oxygen-Reduction Activity on Perovskite Oxide Catalysts for Fuel Cells and Metal-Air Batteries. *Nat. Chem.* **2011**, *3*, 546-50.

(21) Chen, Y.; Ji, S.; Zhao, S.; Chen, W.; Dong, J.; Cheong, W. C.; Shen, R.; Wen, X.; Zheng, L.; Rykov, A. I.; Cai, S.; Tang, H.; Zhuang, Z.; Chen, C.; Peng, Q.; Wang, D.; Li, Y. Enhanced Oxygen Reduction with Single-Atomic-Site Iron Catalysts for A Zinc-Air Battery and Hydrogen-Air Fuel Cell. *Nat. Commun.* **2018**, *9*, 5422.

(22) Wu, G.; Zelenay, P. Nanostructured Nonprecious Metal Catalysts for Oxygen Reduction Reaction. *Acc. Chem. Res.* **2013**, *46*, 1878–1889.

(23) Bhunia, S.; Pena-Duarte, A.; Li, H.; Li, H.; Sanad, M. F.; Saha, P.; Addicoat, M. A.; Sasaki, K.; Strom, T. A.; Yacaman, M. J.; Cabrera, C. R.; Seshadri, R.; Bhattacharya, S.; Bredas, J. L.; Echegoyen, L. [2,1,3]-

Benzothiadiazole-Spaced Co-Porphyrin-Based Covalent Organic Frameworks for O_2 Reduction. *ACS Nano*, **2023**, *17*, 3492-3505.

(24) Yu, M.; Dong, R.; Feng, X. Two-Dimensional Carbon-Rich Conjugated Frameworks for Electrochemical Energy Applications. *J. Am. Chem. Soc.* **2020**, *142*, 12903-12915.

(25) Li, D.; Li, C.; Zhang, L.; Li, H.; Zhu, L.; Yang, D.; Fang, Q.; Qiu, S.; Yao, X. Metal-Free Thiophene-Sulfur Covalent Organic Frameworks: Precise and Controllable Synthesis of Catalytic Active Sites for Oxygen Reduction. *J. Am. Chem. Soc.* **2020**, *142*, 8104-8108.

(26) Miao, Q.; Chen, Z.; Li, X.; Liu, M.; Liu, G.; Yang, X.; Guo, Z.; Yu, C.; Xu, Q.; Zeng, G. Construction of Catalytic Fe_2N_5P Sites in Covalent Organic Framework-Derived Carbon for Catalyzing the Oxygen Reduction Reaction. *ACS Catalysis* **2023**, *13*, 11127-11135.

(27) Wang, D.-G.; Qiu, T.; Guo, W.; Liang, Z.; Tabassum, H.; Xia, D.; Zou, R. Covalent Organic Framework-based Materials for Energy Applications. *Energy & Environmental Science* **2021**, *14*, 688-728..

(28) Singh, S. K.; Takeyasu, K.; Nakamura, J. Active Sites and Mechanism of Oxygen Reduction Reaction Electrocatalysis on Nitrogen-Doped Carbon Materials. *Adv. Mater.* **2019**, *31*, e1804297.

(29) Masa, J.; Xia, W.; Muhler, M.; Schuhmann, W. On the Role of Metals in Nitrogen-Doped Carbon Electrocatalysts for Oxygen Reduction. *Angew. Chem. Int. Ed.* **2015**, *54*, 10102-10120.

(30) Kim, J. H.; Kim, Y.-T.; Joo, S. H. Electrocatalyst Design for Promoting Two-Electron Oxygen Reduction Reaction: Isolation of Active Site Atoms. *Current Opinion in Electrochemistry* **2020**, *21*, 109-116.

(31) Garcia, H.; Roth, H. D. Generation and Reactions of Organic Radical Cations in Zeolites. *Chem. Rev.* **2002**, *102*, 3947-4007.

(32) Fokin, A. A.; Schreiner, P. R. Selective Alkane Transformations via Radicals and Radical Cations: Insights into the Activation Step from Experiment and Theory. *Chem. Rev.* **2002**, *102*, 1551-1593.

(33) Lee, V. Y.; Sekiguchi, A. Stable Silyl, Germyl, and Stannyl Cations, Radicals, and Anions: Heavy Versions of Carbocations, Carbon Radicals, and Carbanions. *Acc. Chem. Res.* **2007**, *40*, 410–419.

(34) Ratera, I.; Veciana, J. Playing with Organic Radicals as Building Blocks for Functional Molecular Materials. *Chem. Soc. Rev.* **2012**, *41*, 303-349.

(35) Kato, K.; Osuka, A. Platforms for Stable Carbon-Centered Radicals. *Angew. Chem. Int. Ed.* **2019**, *58*, 8978-8986..

(36) Chen, Z. X.; Li, Y.; Huang, F. Persistent and Stable Organic Radicals: Design, Synthesis, and Applications. *Chem* **2021**, *7*, 288-332.

(37) Peng, Q.; Obolda, A.; Zhang, M.; Li, F. Organic Light-Emitting Diodes Using a Neutral pi Radical as Emitter: The Emission from a Doublet. *Angew. Chem. Int. Ed.* **2015**, *127*, 7197-7201.

(38) Xiaotian, R.; Ota, W.; Sato, T.; Furukori, M.; Nakayama, Y.; Hosokai, T.; Hisamura, E.; Nakamura, K.; Matsuda, K.; Nakao, K.; Monkman, A. P.; Albrecht, K. Carbazole-Dendronized Luminescent Radicals. *Angew. Chem. Int. Ed.* **2023**, *62*, e202302550.

(39) Tormyshev, V. M.; Bagryanskaya, E. G. Trityl Radicals: Synthesis, Properties, and Applications. *Russian Chemical Bulletin* **2020**, *70*, 278-2297.

(40) Zhang, B.; Mao, H.; Matheu, R.; Reimer, J. A.; Alshmimri, S. A.; Alshihri, S.; Yaghi, O. M. Reticular Synthesis of Multinary Covalent Organic Frameworks. *J. Am. Chem. Soc.* **2019**, *141*, 11420-11424.

(41) Shukla, S.; Mahata, A.; Pathak, B.; Lochab, B. Cardanol Benzoxazines – Interplay of Oxazine Functionality (Mono to Tetra) and Properties. *RSC Advances* **2015**, *5*, 78071-78080.

(42) Moudrakovski, I. L. Recent Advances in Solid-State NMR of Alkaline Earth Elements. *Annual reports on NMR spectroscopy* **2013**, 129-240.

(43) Ardenkjaer-Larsen, J. H.; Boebinger, G. S.; Comment, A.; Duckett, S.; Edison, A. S.; Engelke, F.; Griesinger, C.; Griffin, R. G.; Hilty, C.; Maeda, H.; Parigi, G.; Prisner, T.; Ravera, E.; van Bentum, J.; Vega, S.; Webb, A.; Luchinat, C.; Schwalbe, H.; Frydman, L. Facing and Overcoming Sensitivity Challenges in Biomolecular NMR Spectroscopy. *Angew. Chem. Int. Ed.* **2015**, *54*, 9162-9185.

(44) Karimi, M.; Borthakur, R.; Dorsey, C. L.; Chen, C. H.; Lajeune, S.; Gabbai, F. P. Bifunctional Carbenium Dications as Metal-Free Catalysts for the Reduction of Oxygen. *J. Am. Chem. Soc.* **2020**, *142*, 13651-13656.

(45) Wang, S.; Zhang, L.; Xia, Z.; Roy, A.; Chang, D. W.; Baek, J. B.; Dai, L. BCN Graphene as Efficient Metal-Free Electrocatalyst for the Oxygen Reduction Reaction. *Angew. Chem. Int. Ed.* **2012**, *51*, 4209-4012.

(46) He, T.; Zhao, Y. Covalent Organic Frameworks for Efficient Hydrogen Peroxide Production. *EnergyChem* **2024**, *6*, 100121.

(47) Huang, Z.; Li, M.; Yang, X.; Zhang, T.; Wang, X.; Song, W.; Zhang, J.; Wang, H.; Chen, Y.; Ding, J.; Hu, W. Diatomic Iron with a Pseudo-Phthalocyanine Coordination Environment for Highly Efficient Oxygen Reduction over 150,000 Cycles. *J. Am. Chem. Soc.* **2024**, doi.org/10.1021/jacs.4c05111.

(49) Chen, Y.; Liu, R.; Guo, Y.; Wu, G.; Sum, T. C.; Yang, S. W.; Jiang, D. Hierarchical Assembly of Donor–Acceptor Covalent Organic Frameworks for Photosynthesis of Hydrogen Peroxide from Water and Air. *Nat. Synth.* **2024**, *3*, 998-1010.

(49) Cheng, W.; Su, H.; Liu, Q. Tracking the Oxygen Dynamics of Solid-Liquid Electrochemical Interfaces by Correlative In Situ Synchrotron Spectroscopies. *Acc. Chem. Res.* **2022**, *55*, 1949-1959.

(50) Ma, R.; Lin, G.; Zhou, Y.; Liu, Q.; Zhang, T.; Shan, G.; Yang, M.; Wang, J. A Review of Oxygen Reduction Mechanisms for Metal-Free Carbon-Based Electrocatalysts. *Npj Computational Comput. Mater.* **2019**, *5*, 78.

Graphic entry for the Table of Contents